Numerical analysis of the contemporary interaction between the Phoenix Metro Area Urban Boundary Layer and the local thermo-topographical circulation

Submitted to the Journal of Geophysical Research – Atmosphere

April 3, 2023

A. Brandi[1,2], A. Martilli[2,3], F. Salamanca[1,2], M. Georgescu[1,2]

[1]School of Geographical Sciences and Urban Planning - Arizona State University, Tempe, Arizona, United States of America

[2] Urban Climate Research Center - Arizona State University, Tempe, Arizona, United States of America.

[3] Centre for Energy, Environmental and Technological Research (CIEMAT), Madrid, Spain

Corresponding author: Aldo Brandi (abrandi@asu.edu)

ORCID: 0000-0003-2676-7106

Key Points:

- The thermo-topographical circulation dominates at most times in the complex terrain surrounding Phoenix.
- The built environment of Phoenix Metro acts as a barrier against wind flow as a result of the drag of urban roughness elements.
- The urban heat island of Phoenix Metro does not produce a local circulation with the classical vertical extent, but does interact with the background flow to modulate its intensity.

Abstract

Anthropogenic modification of natural landscapes to urban environments impacts land-atmosphere interactions in the boundary layer. Ample research has demonstrated the effect of such landscape transitions on development of the near-surface urban heat island (UHI), while considerably less attention has been given to impacts on regional wind flow. Here we use a set of high-resolution (1 km grid-spacing) regional climate modeling simulations with the Weather Research and Forecasting (WRF) model coupled to a multi-layer urban canopy scheme to investigate the dynamical interaction between the urban boundary layer (UBL) of the Phoenix Metro (U.S.) area and the thermal circulation of the complex terrain it resides within. We conduct paired simulations for the extremely hot and dry summer of 2020, using a contemporary urban representation and a pre-settlement landscape representation to examine the effect of the built environment on local to regional scale wind flow. Analysis of our simulation results shows that, for a majority of the diurnal cycle, 1) the thermo-topographical circulation dominates, 2) the built environment obstructs wind flow in the inertial sublayer during the nighttime, and (3) the built environment of Phoenix Metro produces an UHI circulation of limited vertical extent that interacts with the background flow to modulate its intensity. Such interaction is modulated by greater daytime urban sensible heat flux and dampens the urban roughness induced drag effect by promoting a deeper UBL through vigorous mixing. Our results highlight the need for future research – both observational and simulation based - into urbanizing regions where multi-scale flows are dominant.

Plain Language Summary

Urban environments alter the natural landscape replacing soil and vegetation with asphalt, concrete and buildings. This kind of modification affects the way the land surface interacts with the overlying atmosphere. The best-known effect of this interaction is the urban heat island effect that consists in a higher temperature within the city compared to the surrounding natural environment. How urban environments interact with the local wind circulation is less understood. With this research we use meteorological simulations to investigate the impact of the current extent of the Phoenix Metropolitan Area (PMA) on the near-surface wind circulation of the complex terrain it resides within during the extremely hot and dry summer of 2020. Results show that the wind circulation in the region is dominated by the effect of topography. In such context, the PMA acts as a barrier that slows down the background wind during most of the day. However, during the morning modest wind acceleration is found upwind of the PMA, as the heat emitted by the built environment reduces the friction produced by its rough morphology. Our results highlight the need for more research upon the interaction between wind flows and urban environments.

Index Terms

0429, 1631, 1632, 3307, 3355

Key Words

Complex terrain UHI circulation urban

1. Introduction

Landscape modifications, such as those associated with urban environments, affect land-atmosphere interactions through modification of the rate and amount of heat, moisture and momentum exchanges in the boundary layer. The best known and most studied consequence of these modifications is the Urban Heat Island (UHI) effect, defined as the difference in air, or surface, temperature between urban environments and their rural surroundings (Oke 1982). Classical conceptual understanding indicates that thermal anomalies represented by the UHI are sufficient to induce a characteristic circulation known as the Urban Heat Island Circulation (UHIC). The UHIC is manifest as rising warm air over the urban core that promotes surface level inflow of cooler air from rural areas (Findlay and Hirt 1969). The UHIC was first observed as early as the 1920s by German meteorologists studying the *Stadtklima* ("*Urban Climate",* Kratzer 1956). Those and several other authors noted that background winds modulated the emergence and intensity of the UHI as well as that of its induced circulation (Chandler 1960). In turn, the UHIC intensity was found to depend on the overall static stability of the urban boundary layer (UBL). Shreffler (1979) used wind records observed during calm days across the city of St. Louis (US), to calculate wind vectors associated with the UHIC and found that a daytime weaker UHI produced stronger circulations than the more intense nocturnal UHI, as daytime instability would favor vertical motion in the UBL. Conversely, a factor likely detrimental to the strength of the nocturnal UHIC is the acceleration of urban surface cooling rates due to the inflow of colder air from the surrounding rural areas (Haeger-Eugensson and Holmer 1999).

Urban environments have distinctive 3D morphologies which increase turbulence in the UBL. The drag effect of buildings can extend up to three times their height (Rafailidis 1997) and acts as a physical barrier against synoptic winds. In 1977, Bornstein and Johnson concluded that wind speed downwind of an idealized representation of New York City would be either increased or decreased by UBL convergence (i.e., the UHIC) and increased roughness, respectively, as a function of background wind speed. Grawe et al. (2013) used non-hydrostatic mesoscale model simulations to show that the Greater London area (UK) can reduce wind speed up to 2.6 m/s in urban areas. Droste et al. (2018) used a conceptual dual column bulk model to show that at specified conditions early afternoon UBL mean wind speed can exceed that of its rural

128 counterpart as a consequence of increased turbulence in the city diluting the drag effect of urban
129 roughness. On the other hand, several studies attribute the globally observed overland decrease
130 in wind speed of the last four decades, also known as wind stilling, to the on-going worldwide
131 urbanization using historical records (McVicar et al. 2011, Chen et al 2020), numerical modeling
132 (Wang et al. 2020) and a combination of both (Hou et al. 2013, Peng et al 2018). As a
133 consequence, a general consensus upon the outcome of the interaction between urban
134 environments and wind flows remains an active area of research.
135
136 The interaction between background wind flow and urban environments can be further
137 complicated for cities located within or surrounded by complex terrain landscapes. In the
138 absence of strong synoptic forcing, surface energy balance differences across the landscape force
139 up-slope/up-valley winds (also known as *anabatic*) during the daytime and down-slope/down-
140 valley (*katabatic*) winds at nighttime (Blumen 2016). Thermal circulations can have detrimental
141 impacts for cities located in complex terrain as the anabatic and katabatic wind regimes are
142 partitioned by the morning and evening transitions (i.e., times of low wind speed and a lack of a
143 predominant wind direction preceding flow reversal). Transitions tend to happen during rush
144 hour traffic, hindering effective dispersion of vehicular pollutant emission (Fernando 2010). In
145 addition, katabatic winds can be detrimental for air quality of cities located at the bottom of
146 valleys as they tend to generate lapse rate inversions that suppress vertical motion by building up
147 cold air pools (Monti et al. 2002).
148
149 Here we use a set of two four-month long (MJJA), summertime, Weather Research and
150 Forecast (WRF, Skamarock et al. 2019) model high resolution simulations to investigate the
151 interaction between boundary layer dynamics over the Phoenix Metropolitan Area (PMA),
152 Arizona, U.S., and the wind circulation of the complex terrain it resides within. We choose
153 Phoenix as our testbed as it is the fastest growing and fifth largest U.S. city (Bureau 2019) and is
154 a natural proving ground for urban climate research (Chow et al., 2012). Located within the
155 southwestern US, the PMA is located in complex terrain and its summertime climatology is
156 characterized by persistent high-pressure systems and low synoptic winds (Balling and Cerveny
157 1984). The Phoenix Valley extends on a northwest-southeast axis, is surrounded by steep
158 mountain ranges to the north and east, and by smaller reliefs to its southwest (inset, Fig. 1).

Valley slopes are generally shallow in the area (<0.5^{o}) and average winds flow along the central valley with westerly orientation during daytime and easterly at nighttime (Brazel et al 2005). The lack of tall vegetation in the non-built areas (the surrounding semi-desert is primarily composed of xeric shrubs; Georgescu et al., 2008) surrounding the city is expected to highlight the differences in aerodynamic and more generally, biophysical, properties between the two landscapes. For example, the PMA frequently displays a daytime negative UHI effect, which has been attributed to the combined effects of enhanced heat storage within the urban landscape and greater warming rates across the surrounding semidesert biome (Georgescu et al. 2011). Such characteristics are expected to affect the UHI circulation of metro Phoenix by reducing its intensity during the daytime. Balling and Cerveny (1987) found a 60% observed increase in mean monthly wind speed in Phoenix between 1948 and 1985 and suggested a strong dependency on the growing UHI over the city. The thermal circulation in the Phoenix metro valley has also been the subject of several meteorological studies. Three major experimental campaigns, The Phoenix AirFlow Experiments (PAFEX-I and PAFEX-II, Fernando et al. 2001) and the Transition Flow Experiment (TRANSFLEX, Fernando et al. 2013), were conducted in the area in the late 1990s and early 2000s. These campaigns measured the impact of the local thermal circulation on air quality in the PMA with a focus on the morning and evening transitions (Fernando et al. 2010). Prior research has also examined impacts of land use and land cover (LULC) change on the surface energy balance of the PMA (Georgescu et al. (2009), using mesoscale simulations with the RAMS model, by incorporating realistic representations of three different historical landscapes to investigate the role of urban development on local landscape heterogeneity induced mesoscale circulations. Georgescu et al. (2009a and 2009b) showed that nearly three decades of transitioning from agricultural and natural shrub to urban landscapes generated strong thermal and moisture gradients across the valley, resulting in increased wind speed and dryness in the lower UBL and increased moisture in the upper BL.

In order to better understand the impact of urban environments on climate, it is important to improve the representation of urban landscapes through enhanced multi-scale process-based representation (Sharma et al. 2021). While considerable research has studied the interaction between UHIC and sea breeze circulations (Cenedese and Monti 2003, Ohasi and Kida 2002, Ryu and Baik 2013), the few studies investigating the interaction between the UHIC and thermo-topographical circulations in complex terrain have done so through numerical simulation of

idealized cases (Savijärvi and Liya 2001, Ganbat et al. 2015). Our analysis of the scientific literature indicates there are no mesoscale modeling studies examining urban climate modification of flow with realistic representation of urban areas and meteorological forcing (Wu et al. 2021). Throughout history, complex terrain offered the benefit of ample water resources and tactical defense advantages to human settlements, resulting in a greater abundance of urban environments compared to other landscapes. Here, we investigate the diurnal evolution of UBL dynamics in complex terrain at high spatial and temporal resolution by comparing simulation results from two numerical experiments. The first one features a realistic representation of the current extent of the PMA; the second represents a hypothetical pre-settlement scenario where no anthropogenic modification to the landscape exists. Our work fills a gap in urban climate research by improving the understanding of a rarely investigated component of urbanization impacts. In addition to the scientific merit, improved understanding of urban environmental effects and potential interactions with local and regional wind flows has relevant implications for aviation operations and assessment of pollutant dispersion and transport.

The paper is organized as follows: Section 2 describes the model configuration, the datasets used to drive the simulations and the comparison scenarios. Section 3 presents the analysis results. Finally, Section 4 draws conclusions and discusses potential impacts, limitations, and future research.

2. Data and Methods

WRF is a highly customizable weather and climate model that has been successfully used to study wind flows over urban environments in complex terrain (Papanastasiou et al 2010, Giovannini et al. 2014, Puliafito et al 2015, Toro et al. 2019), including the Phoenix region (Li et al. 2015, Foroutan and Pleim 2017). In this study, we use WRF version 4.2.2, and employ a three-domain one-way nested configuration centered over the Phoenix Sky Harbor International Airport (33°25'48.0"N 112°00'00.0"W) with grid spacing of 9, 3, and 1 km for the outermost, intermediate, and innermost domain, respectively. The vertical direction is discretized into 50 model levels of increasing thickness with height. The top of the lowest model level is at 50 meters above the surface and its mass center is around 25 m above ground level (AGL) to capture dynamic interactions within the inertial sublayer (ISL; i.e., more than twice the average

building height). Initial and boundary conditions for our simulations were provided by the NCEP North American Regional Reanalysis (NARR, Mesinger et al. 2006) dataset. We focus our analysis on the summer (June, July and August; JJA) of the year 2020 to remove potential confounding complications arising from the convective storm regime typical of the Northern American Monsoon season (Vera et al. 2006). We note that this summer was one of the driest during the last 30 years (1993-2023) for Arizona, with a total statewide average cumulative precipitation of only 46 mm (NOAA, Climate at a glance).

LULC and impervious fraction cover data were extracted from the National Land Cover Database 2019 (NLCD) which consists of 40 land cover categories and also includes impervious cover data. This information is retrieved by the Landsat Thematic Mapper satellite sensor and is validated against high resolution aerial photographic products (Jin et al. 2021). We resampled the NLCD dataset from the original 30 m spatial resolution to the innermost WRF domain grid spacing of 1 km using ArcMap 10.8 software (Esri 2011) for ingestion in the *geogrid* module of the WRF Preprocessing System (WPS, Skamarock et al. 2019). Such a procedure was found to improve the land cover representation in the WRF model as opposed to directly ingesting native resolution NLCD 2019 data in *geogrid*. In the NLCD 2019 classification, the PMA consists of two urban land cover categories: 25 – Medium Intensity Development, and 26 – High Intensity Development (Figure 2a).

Urban land surface energy and momentum fluxes are dynamically calculated by the coupled Building Effect Parameterization and Building Energy Model (BEP-BEM, Martilli et al., 2002; Salamanca et al. 2010). BEP-BEM explicitly computes energy exchanges between the outdoor air and building roofs and walls, as well as the heat resulting from air conditioning systems use, an important feature of the urban canopy climate in a hot desert conurbation like Phoenix metro. In order to attain a more realistic representation of the urban land cover of the PMA, we modified a number of biophysical parameters of urban materials in the URBPARM.TBL file of the WRF model (Table 1) and derived the statistical distribution of building heights from the latest available urban morphology assessment (Burian et al. 2002). Although somewhat older, such a dataset remains representative, as the abundance of barren land in the area favors low-rise housing development in addressing the continued population growth. Rural land surface, and soil heat and moisture fluxes are treated by the Noah Land Surface Model (Chen and Dudhia 2001). Land surface fluxes and the overlying atmosphere are coupled

by the Mellor-Yamada-Janjić Planetary Boundary Layer scheme (MYJ PBL, Mellor and Yamada 1982, Janjic 2001) wherein the PBL height is calculated as a function of turbulent kinetic energy (TKE). Simulation output is stored at hourly frequency for the entire simulation period.

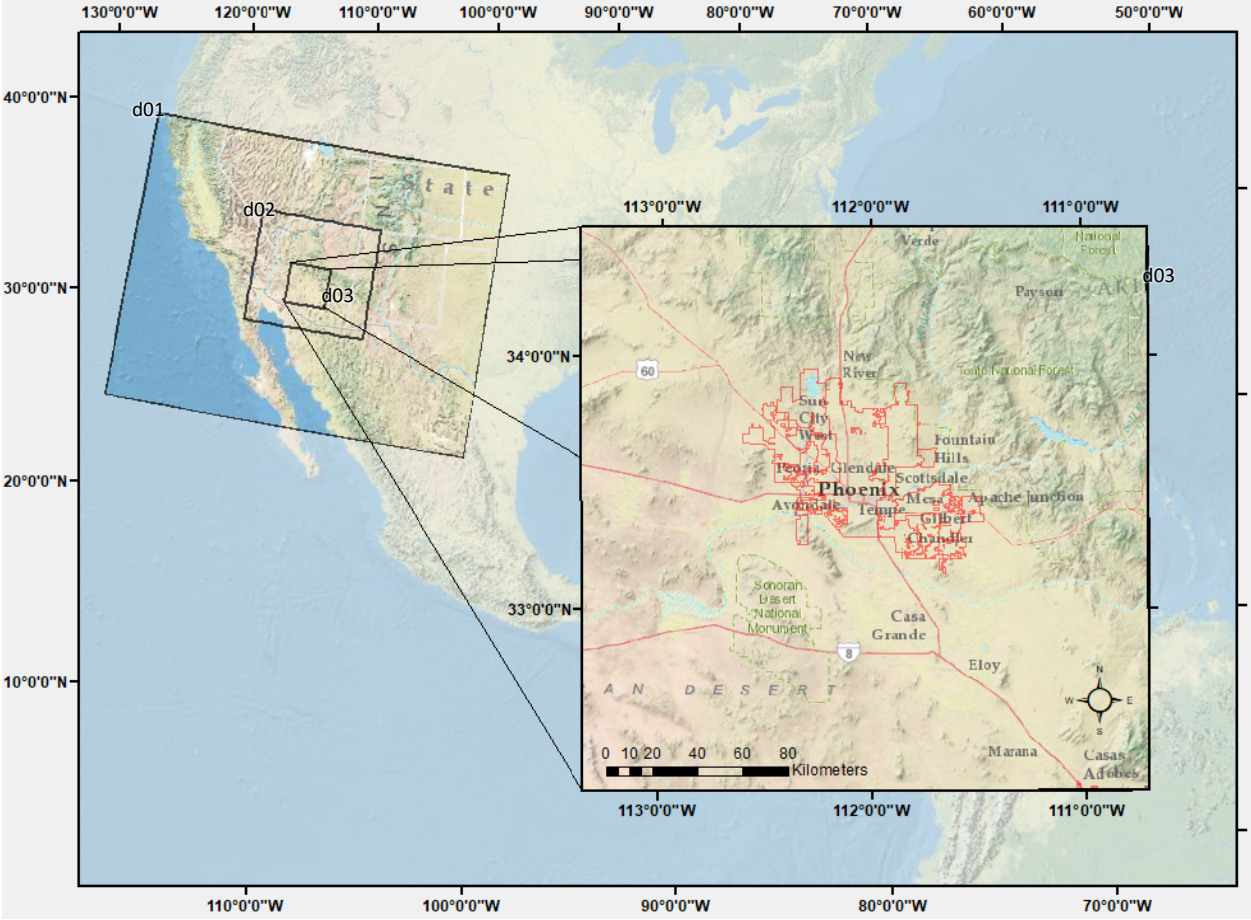

Fig. 1 Geographical location of the three nested simulation domains. Inset: innermost domain with representation of the Phoenix Metro Area (red outline) and the complex terrain it resides within.

Table 1.

List of parameters modified in the URBPARM.TBL file.

Parameter	Low and High Intensity Residential
CAPR: Heat capacity of roofs[1]	1.82×10^6 [J m^{-3} K^{-1}]
CAPB: Heat capacity of walls[1]	1.82×10^6 [J m^{-3} K^{-1}]
CAPG: Heat capacity of ground/road[2]	1.74×10^6 [J m^{-3} K^{-1}]

Note. Modifications introduced to improve representation of thermal characteristics of the Phoenix urban fabric. Roofs and walls are assumed to be made of concrete, roads of asphalt. [1]Laloui and Loria (2019). [2]Li et al. (2021)

In order to assess the impact of the current extent and nature of Phoenix metro's urban expansion on wind circulation, we conducted paired simulations with identical meteorology driven by two LULC scenarios. Both simulations are initialized on May 1st, 2020, at 00:00 UTC and terminated on August 31st, 2020, at 00:00 UTC. The first month of simulation, i.e., from May 1st to May 30th, 2020, is considered as spin-up time and is not included in the analysis of results. The simulation time-step is set to 25 seconds in the outermost domain and it is subsequently downscaled to the intermediate and innermost domains by a ratio of 3. The first simulation, henceforth referred to as *Control*, reproduces the current LULC extent and characteristics of PMA and its surrounding valley (Figure 2a). The second simulation, henceforth referred to as *Pre-Settlement*, reproduces a situation where no anthropogenic landscape modification exists, whereby all urban (categories 25 and 26) and agricultural (category 38 – Crops) pixels were replaced with the dominant natural land cover category in the semi-desert valley (category 32 – Shrubs/Scrubs, Figure 2b). Such a replacement results in a decrease in background roughness length (Z_0) across the extent of the urban area relative to the *Control* scenario, from 1.5 m (i.e., category 25, or medium intensity development) and 2.0 m (i.e., category 26, or high intensity development) to 0.3 m (i.e., category 32) in the *Pre-Settlement* scenario. In addition, in the *Pre-Settlement* scenario, the impervious fraction cover was set to zero everywhere.

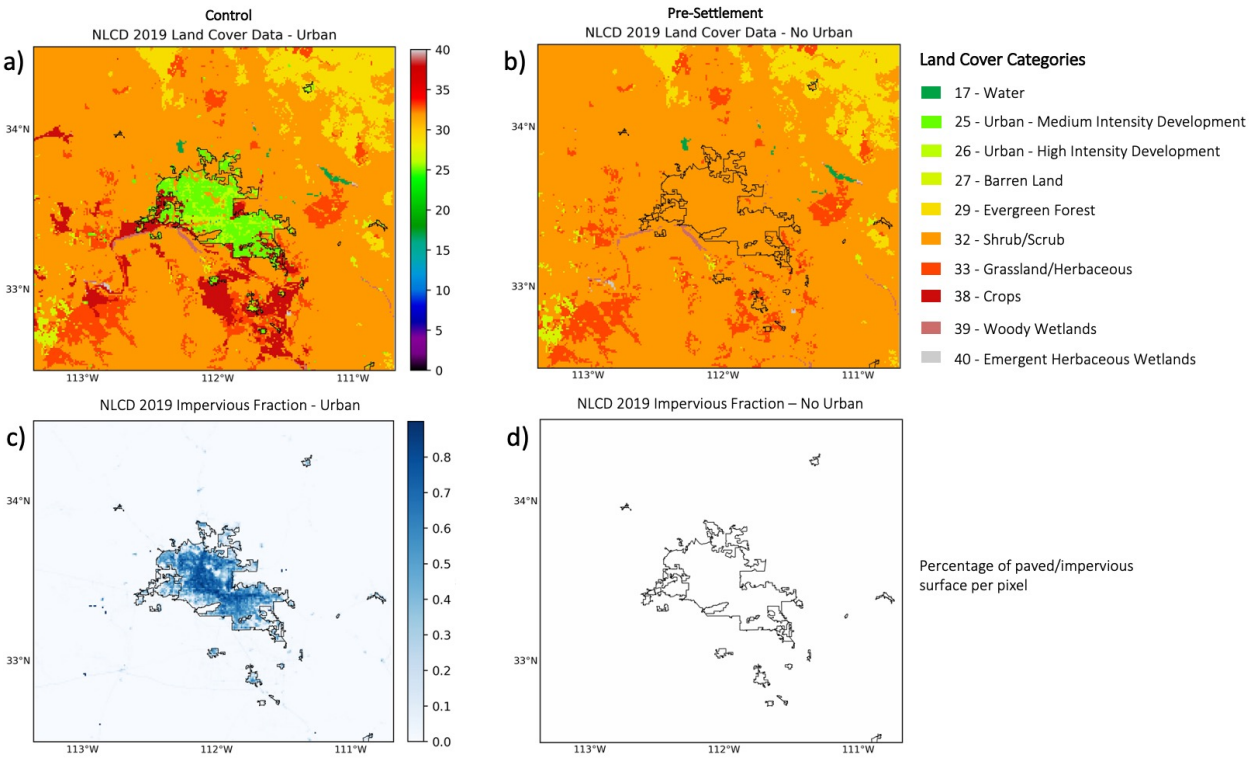

Fig. 2 Land cover categories used in the **a)** *Control* and **b)** *Pre-Settlement* scenarios. Urban Fraction cover used in the **c**) *Control* and **d**) *Pre-Settlement* scenarios.The outline (black) of the urban area is retained in panels b) and d) for reference.

We evaluate our *Control* simulation against a set of ground observations, both within and outside of the PMA urban area (Fig. 3), and against satellite observations. Given the eolian focus of this study and the choice of the extremely dry summer of 2020 as the study period, we center our assessment of model performance on air and land surface temperature as well as wind speed and direction.

Ground observations for model evaluation are retrieved from two networks of automated weather stations producing publicly available data: the Arizona Meteorological Network (AZMET, Brown and Russel 1987-1995), operated and maintained by the University of Arizona, and the National Weather Service Automated Surface Observing System network (NWS ASOS, Nadolski 1998). To evaluate model results within the urban area we use two AZMET stations, located in city parks, and three ASOS stations, located at airports, whereas we use four AZMET stations for the evaluation of rural results. Model evaluation is performed by comparing hourly observed and simulated values averaged across stations and corresponding model cells, respectively. Finally, daytime (13:00 LT) and nighttime (22:00 LT) land surface temperature

(LST) observations were obtained from the MODIS/Terra (MOD11A1 V6.1 product, Wan et al. 2020) and processed with Google Earth Engine (Gorelick et al. 2017). LST satellite observations were averaged across the entire simulation period (JJA) and compared to JJA averages of corresponding daytime and nighttime Surface Skin Temperature (TSK) model output.

a)

Station name	Latitude	Longitude	Elevation	Classification	Network
Phoenix/Sky Harbor	33.43	-112.01	337	Urban	ASOS
Luke AFB/Phoenix	33.53	-112.38	332	Urban	ASOS
Deer Valley/Phoenix	33.69	-112.08	450	Urban	ASOS
Phoenix Encanto	33.48	-112.1	334	Urban	AZMET
Phoenix Greenway	33.62	-112.11	403	Urban	AZMET
Harquahala	33.49	-113.11	384.4	Rural	AZMET
Coolidge	32.98	-111.61	423	Rural	AZMET
Queen Creek	33.19	-111.53	462	Rural	AZMET
Paloma	32.93	-112.9	221	Rural	AZMET

b)

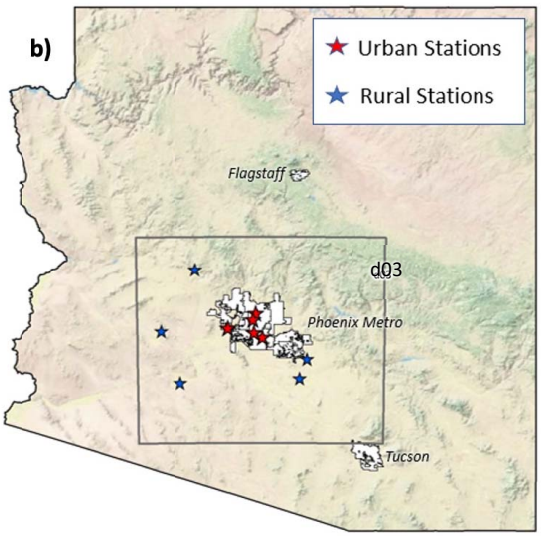

Fig. 3 List **a)** and spatial distribution **b)** of the weather stations used for evaluation of Control simulation. Red stars represent urban stations, and blue stars represent rural stations. The dark gray rectangle represents the extent of the innermost simulation domain (d03).

3. Results

3.1 Model Evaluation

The WRF model successfully reproduces the diurnal and seasonal cycles of 2 m air temperature in the urban area of Phoenix: we calculate a root mean square error (RMSE) of 2.24 K and a mean absolute error (MAE) of -0.68K when comparing hourly observations and model output for the three-month extent of the simulation (Fig. 4a). Overall, urban air temperature maxima are better reproduced than minima: the model simulates a systematically longer nighttime cooling lag of 2-3 hours over urban cells than what was observed at weather stations, leading to a seasonally averaged peak cool bias of -7 K at 7:00 AM local time (Fig. 4c). When comparing diagnosed WRF 2 m air temperature values with rural area observations, the RMSE

and MAE scores are similar to those obtained over urban areas (Table 2), although the bias is positive and peaks at 3 K at 4:00 PM (not shown). Land surface temperature differences between observed and simulated values are greater, especially during the daytime (Table 2). Across the innermost simulation domain, the average MAE associated with calculated land surface temperature differences between the WRF model and MODIS observations is 2.43 K during the daytime (13:00 LT, RMSE = 4.58 K) and 1.8 K at nighttime (10:00 LT, RMSE = 3.22 K). Comparison of 10 m wind speed and direction (the latter assessed through decomposition of the wind vector in U and V components, Table 2) shows that the WRF model, although slightly overestimating maximum wind speed, accurately reproduces its diurnal evolution throughout the entire simulation period (Fig. 4b and 4d). RMSE and MAE range between 1.56 m/s and -0.36 m/s (Table 2). Analysis of our simulation results provides confidence in the model's ability to correctly reproduce wind flow dynamics and characteristics within and around the PMA. Evaluation results are summarized in Table 2, and overall show a general agreement with those of Salamanca et al. (2018) whose work examined the skill of different configurations of the WRF model to correctly simulate the meteorology of the PMA conurbation.

Table 2

List of Model Evaluation Results.

Variable	RMSE	MAE
2m Air Temperature - Urban (Time series)	2.24 K	-0.68 K
2m Air Temperature - Rural (Time series)	2.16 K	0.26 K
2m Air Temperature – Urban (Diurnal composite)	3.27 K	2.27 K
2m Air Temperature – Rural (Diurnal composite)	1.8 K	1.09 K
10m Wind Speed – Urban (Time series)	1.29 m/s	0.47 m/s
10m Wind Speed – Rural (Time series)	1.56 m/s	1.05 m/s
10m Wind Speed – Urban (Diurnal composite)	0.68 m/s	-0.36 m/s
10m Wind Speed – Rural (Diurnal composite)	1.44 m/s	1.24 m/s
10m U component – Urban (Time series)	2.74 m/s	1.41 m/s
10m V component – Urban (Time series)	1.86 m/s	0.78 m/s
10m U component – Rural (Time series)	2.74 m/s	1.22 m/s
10m V component – Rural (Time series)	2.15 m/s	1.20 m/s
Land Surface Temperature (Daytime, 1300 LT)	4.58 K	2.43 K
Land Surface Temperature (Nighttime, 2200 LT)	3.22 K	1.80 K

Note. Time series scores are calculated comparing hourly averages of station observations and corresponding model cell values throughout the entire simulation period (JJA). Diurnal cycle scores are calculated comparing hourly JJA averages of station observations and corresponding model cell values. Land Surface Temperature scores are calculated comparing daytime (11:00 AM local time) and nighttime (10:00 PM local time) satellite data and Skin Temperature (TSK) values from WRF averaged throughout the innermost domain and the entire simulation period.

Fig. 4 Summary of validation results. **a)** Time series of 2m air temperature hourly observation and WRF model output. **b)** Time series of 10 m wind speed observations and WRF model output. **c)** Diurnal composite of JJA 2 m air temperature observations and WRF model output. **d)** Diurnal composite of of JJA 10 m wind speed observations and WRF model output. All panels: black lines represent observed values averaged across all 5 weather stations; red lines represent WRF model output averaged across the 5 most closely corresponding model cells. Blue lines represent the difference WRF – Obs. Shaded areas represent 1σ of the average.

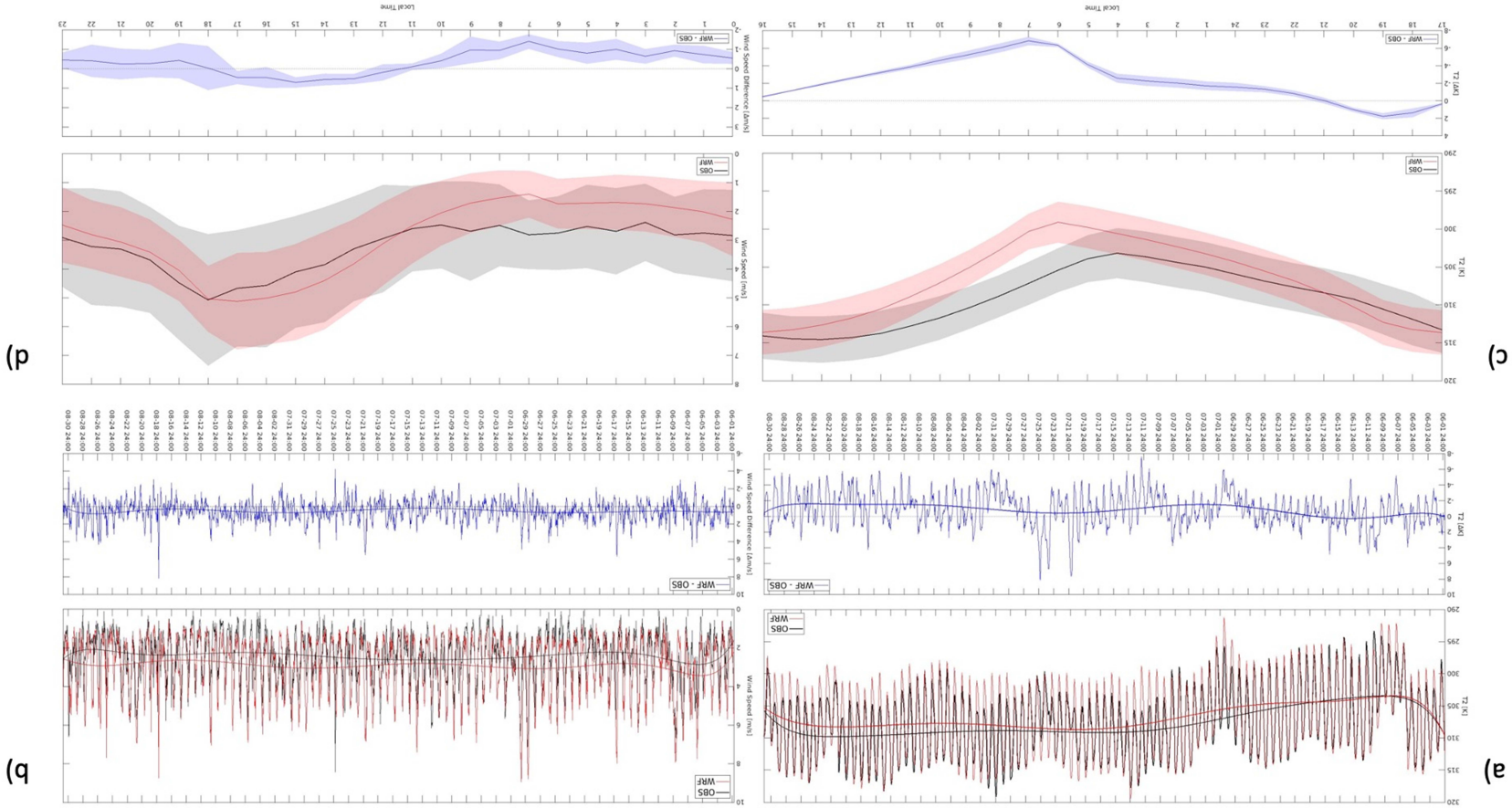

367 *3.2 Thermal circulation in a Pre-Settlement landscape*

368

369 In the absence of any anthropogenic modification to the natural complex terrain landscape the
370 Phoenix urban environment resides within, boundary layer wind flow patterns, when averaged
371 across the entire simulation period (JJA), closely follow the prescribed oscillation between
372 anabatic and katabatic regimes of thermal circulations (Fig. 5). Timing of flow reversal changes
373 between the low plains in the central and southwest portions of the simulation domain and the
374 steep slopes to the north and the east of the PMA, as elevation gradients either support or oppose
375 downslope and upslope inertial flows, respectively. Here, morning and evening transition times
376 are visually assessed throughout the simulation domain as the times showing the least signs of
377 organized thermo-topographic flows. The cycle starts at 8:00 AM local time (LT) when the lack
378 of a predominant wind direction and the lowest wind speed of the diurnal cycle (1.44 m/s on
379 average across the innermost domain and the entire simulation) marks the onset of the morning
380 transition (Fig. 5a). At this time, the wind flow is southeasterly in the northwest portion of the
381 innermost domain, southwesterly over the Colorado Plateau to the northeast of the PMA and
382 strongly southerly across the southwest portion of the study area. Wind speed is generally low
383 (1-2 m/s) within the narrow valleys of the Mogollon Rim to the north and upwind of major
384 reliefs. Starting at around 9:00 AM LT, as the surface warms up, up-valley and up-slope winds
385 begin to develop until the maximum intensity of the anabatic regime (6.75 m/s) is attained at 11
386 AM LT (Fig. 5b). At this time, wind flow is southerly across the entire east end of the domain
387 and along the narrow valleys of the Mogollon Rim, southwesterly over the eastern portion of the
388 simulation domain. Starting at around 12:00 PM LT, the strength of the anabatic regime begins
389 decaying as the southwesterly anticyclonic synoptic flow increases in magnitude. During the
390 afternoon, topography exerts less and less impact on an increasingly stronger and southwesterly
391 wind flow. At 7:00 PM LT the magnitude of the airflow begins to decrease along the west facing
392 slopes of the narrow valley along the Mogollon Rim, as flow reversal marks the onset of the
393 evening transition (Fig. 5c). Flow reversal then initiates at around 8:00 PM LT as down-slope
394 winds in the narrow valleys of the Mogollon Rim to the north and along the west and south
395 facing steep slopes of the mountains to the east. When, at around 11:00 PM LT, down-slope
396 flows appear on the southeast quadrant of the domain, the combination of these three draining air
397 streams promotes flow reversal in the central part of the valley. The resulting easterly down-

valley flow continues to increase throughout the night until 6:00 AM LT, when the overall katabatic regime reaches its peak intensity (Fig. 5d).

The only region that remains virtually undisturbed throughout the diurnal cycle is the southwestern quadrant along the Colorado Plateau, towards the northeast portions of the domain, where winds remain consistently aligned with the synoptic southwesterly flow at all times.

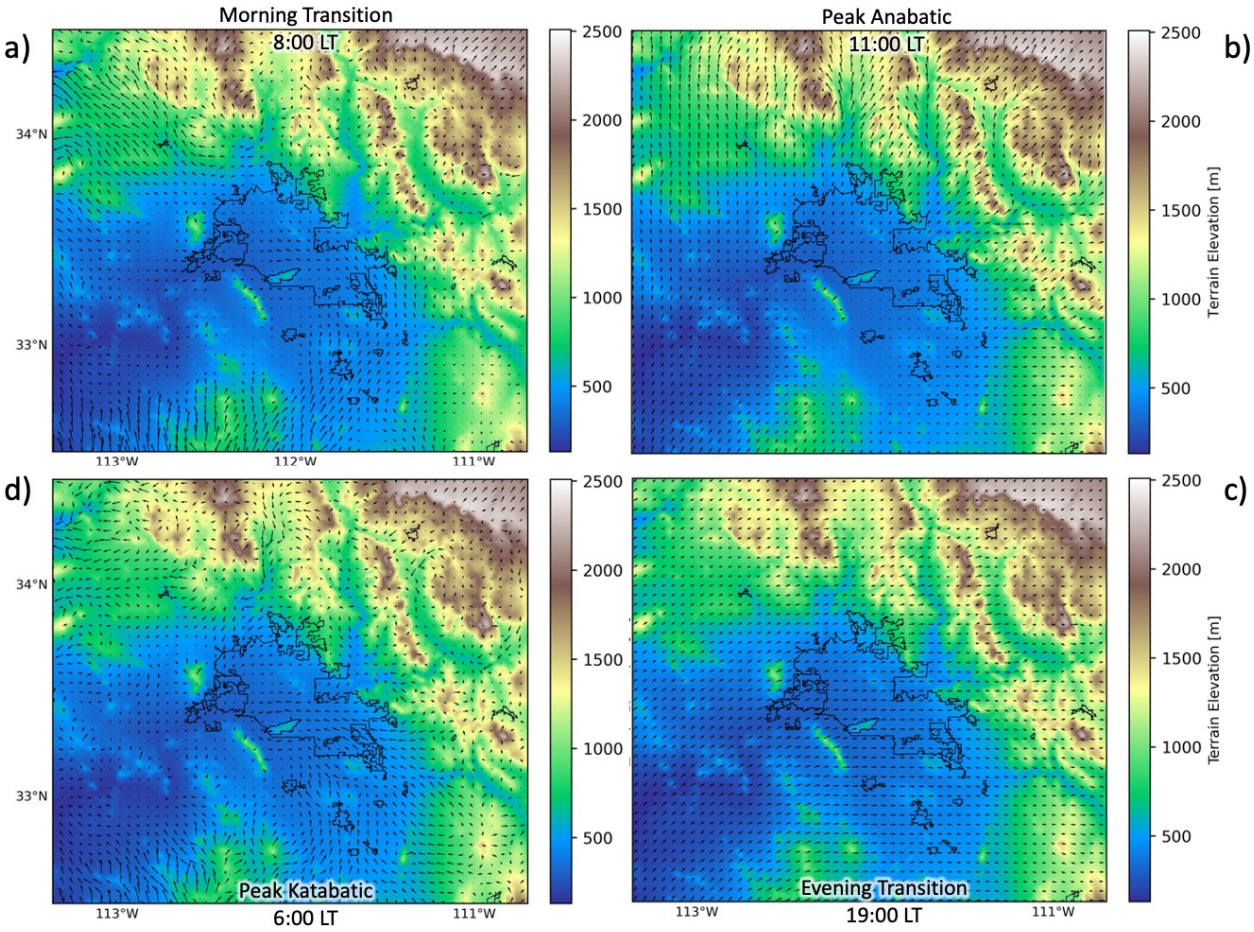

Fig. 5 JJA average of *Pre-Settlement* scenario first model level (25 m AGL) wind vectors in the innermost simulation domain (d03). Color shading represents the local topography. The current urban extent of the PMA (black outline) is provided for reference.

3.3 Urban impacts on wind speed

Despite an average building height between 5 and 10 m across the vast majority of the PMA, the city mostly acts as a physical barrier against wind flow throughout the diurnal cycle (Fig. 6).

The only exception consists of a few hours during the morning (between 9:00 AM and 12:00 PM LT), when the wind flow over the urban area remains virtually undisturbed (Fig. 6b). Throughout the rest of the day, regardless of wind direction, the urban environment of Phoenix metro exerts a drag on wind speed within, and at times also downwind of, the city (Fig. 6c). Wind speed differences between the *Control* and *Pre-Settlement* scenarios (averaged over the urban area) range from a minimum reduction of -0.1 m/s (-1.5% at 12:00 PM LT) to a maximum of -0.92 m/s (-45.54 % at 6:00 AM LT). Wind speed reduction in the first model level (i.e., within the ISL) over the PMA is negatively correlated to the magnitude of sensible heat flux excess in the urban environment compared to *Pre-Settlement* values ($y = -0.0059x$, $R^2 = 0.512$).

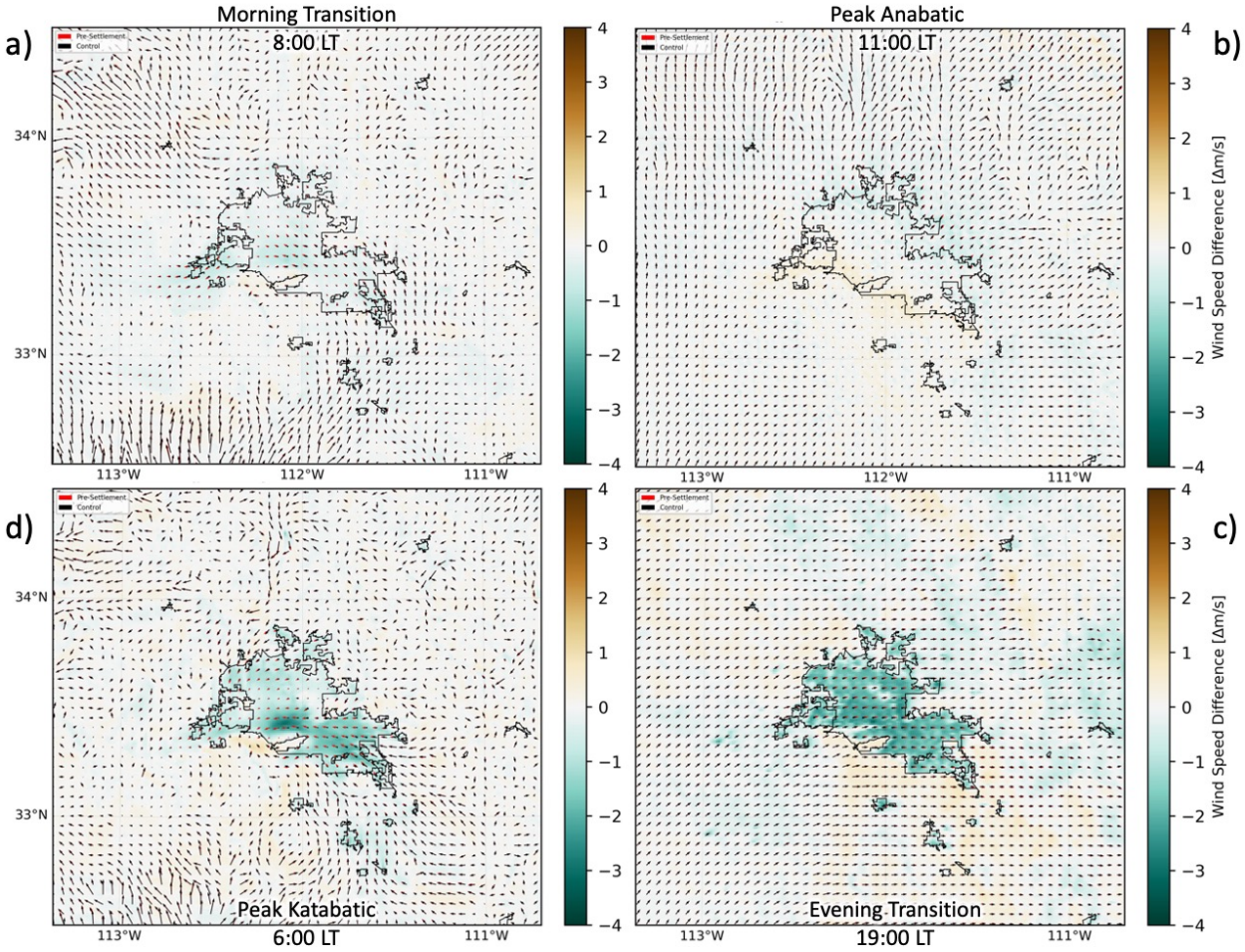

Fig. 6 JJA average of *Pre-Settlement* (red arrows) and *Control* (black arrows) simulation first model level (25 m AGL) wind vectors in the innermost simulation domain (d03). Color shading represent the wind speed difference *Control - Pre-Settlement*.

The negative correlation between urban sensible heat flux and drag effect on wind speed is the result of increased mixing in the UBL. Daytime urban sensible heat flux across Phoenix is greater than at nighttime, resulting in a well-developed daytime UBL and strong mixing that dilutes the friction exerted by the shallow urban canopy layer. The diurnal cycle of urban sensible heat flux interacts with the background wind speed in modulating the impact of the conurbation on boundary layer winds (Fig. 6). During the daytime the excess of sensible heat flux over the PMA (calculated as a difference between the *Control* and *Pre-Settlement* scenarios across all urban cells) ranges between +79.38 W/m^2 at 9:00 AM LT and +141.66 W/m^2 at 1:00 PM. This evolution results in average UBL depths of 466.15 m and 1692.67 m AGL, respectively and minimal average wind speed reductions of up to -0.1 m/s (-8%). During the late afternoon (from 4:00 PM to 5:00 PM LT) the excess of urban sensible heat flux sharply drops from +101.33 to +64.4 W/m^2 and continues to decrease throughout the evening, reaching an average value of +6.84 W/m^2 at 9:00 PM LT. Simultaneously, background wind speed over the urban area consistently reaches speeds at or above 5 m/s, resulting in wind speed reductions of ~ -1.55 m/s (-30% at 7:00 PM at a UBL depth of 721.1 m AGL; Table S1). During nighttime, urban sensible heat flux excess remains below +10 W/m^2, resulting in an extremely shallow UBL (from 350 m AGL at 9:00 PM to <100 m AGL at 6:00 AM). The combination of low urban sensible heat flux excess and low wind speed results in the greatest relative wind speed reductions over the urban area of the entire diurnal cycle (-7 m/s ca. ~ -40%, Fig. 7 and Table S1).

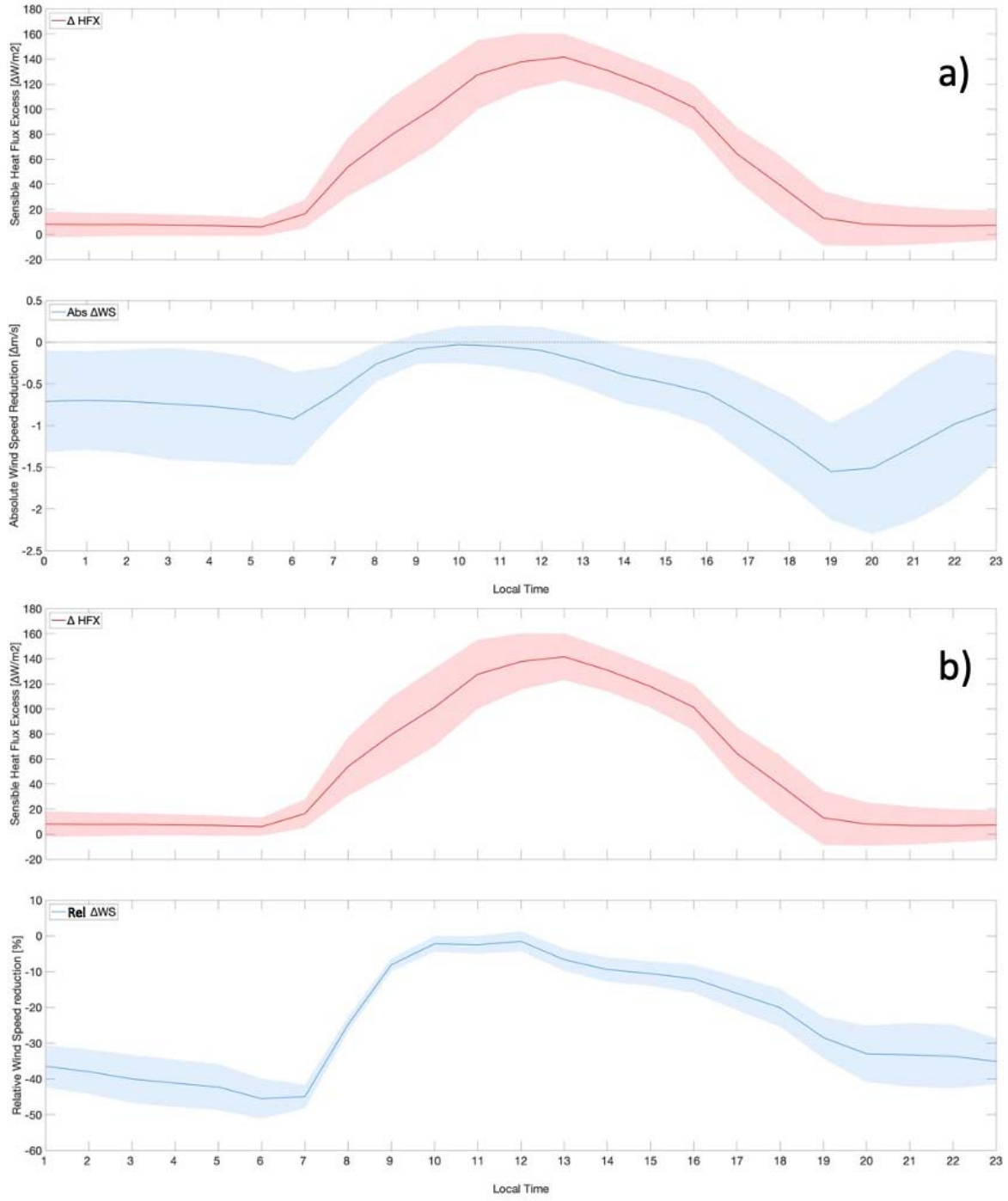

Fig. 7 a) Diurnal composite of JJA averaged urban sensible heat flux excess (*Control* – *Pre*-Settlement) and first model level (25 m AGL) absolute wind speed reduction (*Control* – *Pre*-Settlement). **b) D**iurnal composite of JJA averaged urban sensible heat flux excess (*Control* – *Pre*-Settlement) and first model level (25 m AGL) relative wind speed reduction (*Control* – *Pre*-Settlement)

Throughout the night and the early morning (from 10:00 PM to 6:00 AM LT) the combination of excess sensible heat flux lesser than +10 W/m^2 and a background wind speed around 2 m/s hinders the production of turbulence in the shallow, stable, nighttime UBL. This results in TKE differences between the *Control* and *Pre-Settlement* over the current extent of the urban area ranging between +0.11 m^2/s^2 at 10:00 PM and 0 m^2/s^2 at 6:00 AM LT (Fig. 8c). During the morning, despite a background wind speed still below or at 2 m/s over the urban area, the TKE difference, although small at ~ 0.2 m^2/s^2 (Fig. 8f), remains positive due to an excess of urban sensible heat flux of +101.28 W/m^2 at 10:00 AM (Fig. 8e). Between 2:00 and 4:00 PM LT, TKE differences reach their maximum value of +0.4 m^2/s^2 as a result of greater sensible heat flux excess (around and above +100 W/m^2) and greater background wind speed (4-5.5 m/s). At 6:00 PM LT, despite an average excess of urban sensible heat flux as low as +39.24 W/m^2 (Fig. 8h), a strong background wind reaching 5.93 m/s sustains TKE production at +0.39 m^2/s^2 via intense wind shear (Fig. 8i).

3.4 UHI induced circulation

Figure 9 shows air temperature differences between the *Control* and *Pre-Settlement* scenarios across the entire innermost domain (d03) at 2 and 26 meters AGL. In agreement with previous results (Georgescu et al., 2011), throughout the daytime (from 7:00 AM to 5:00 PM LT) an Urban Cool Island effect (UCI, also known as the *Oasis Effect*) is observed over the PMA, with a maximum 2 m air temperature difference of -1.16 K at 2:00 PM (Fig. 9a). At nighttime (from 7:00 PM to 6:00 AM LT) the classic UHI effect is present with a maximum 2 m air temperature difference across the urban area of +2.62 K at 8:00 PM (Fig. 9b). The calculation of the UHI above the near-surface (i.e., at the mass center of the first model level at 26 m AGL) reveals a different result.

Although rather weak, at the time of peak magnitude of the 2 m UCI, air temperature in the first model layer (25 m AGL) is greater in the *Control* scenario than in the *Pre-Settlement* scenario (+0.49 K on average above the urban area) thus highlighting a UBL heat island (UBLHI) that extends to around 1700 m AGL (not shown) as a consequence of strong mixing. Throughout the night, the UBLHI effect intensifies in magnitude, reaching its peak intensity of +0.79 K at 9:00 PM LT (Fig. 9d) while decreasing in vertical extent to around 200 m AGL, at times extending

for several tens of meters above the diagnosed UBL depth in the early morning hours (from 3:00 to 7:00 AM, Fig. 10d).

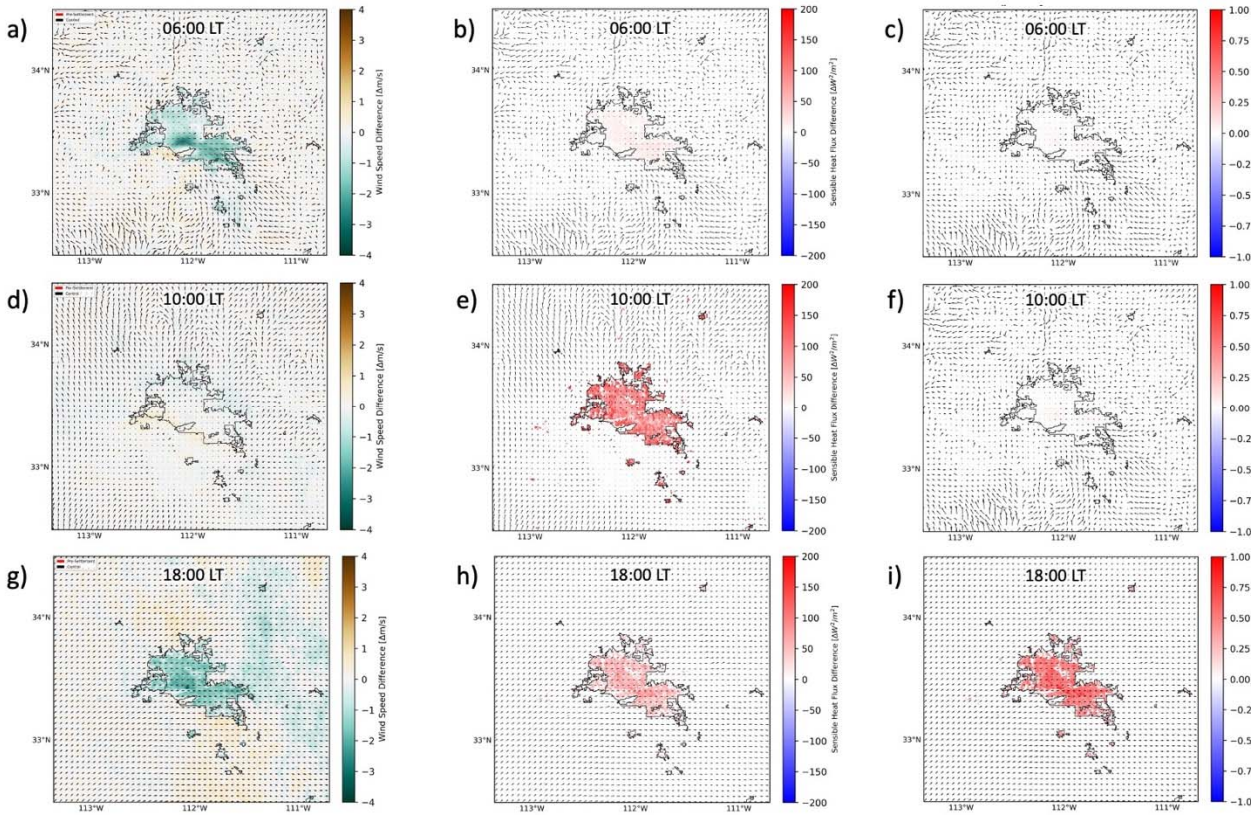

Fig. 8 Simulated JJA averaged **a)** wind speed **b)** sensible heat flux and **c)** TKE differences between the *Control* and the *Pre-Settlement* scenarios at 6:00 AM LT. **d)**, **e)**, **f)** same as **a)**, **b)**, **c)** but at 10:00 AM LT. **g)**, **h)**, **i)** same as **a)**, **b)**, **c)** but at 6:00 PM LT. All panels: black arrows represent JJA average of *Control* scenario first model level (25 m AGL) wind vectors.

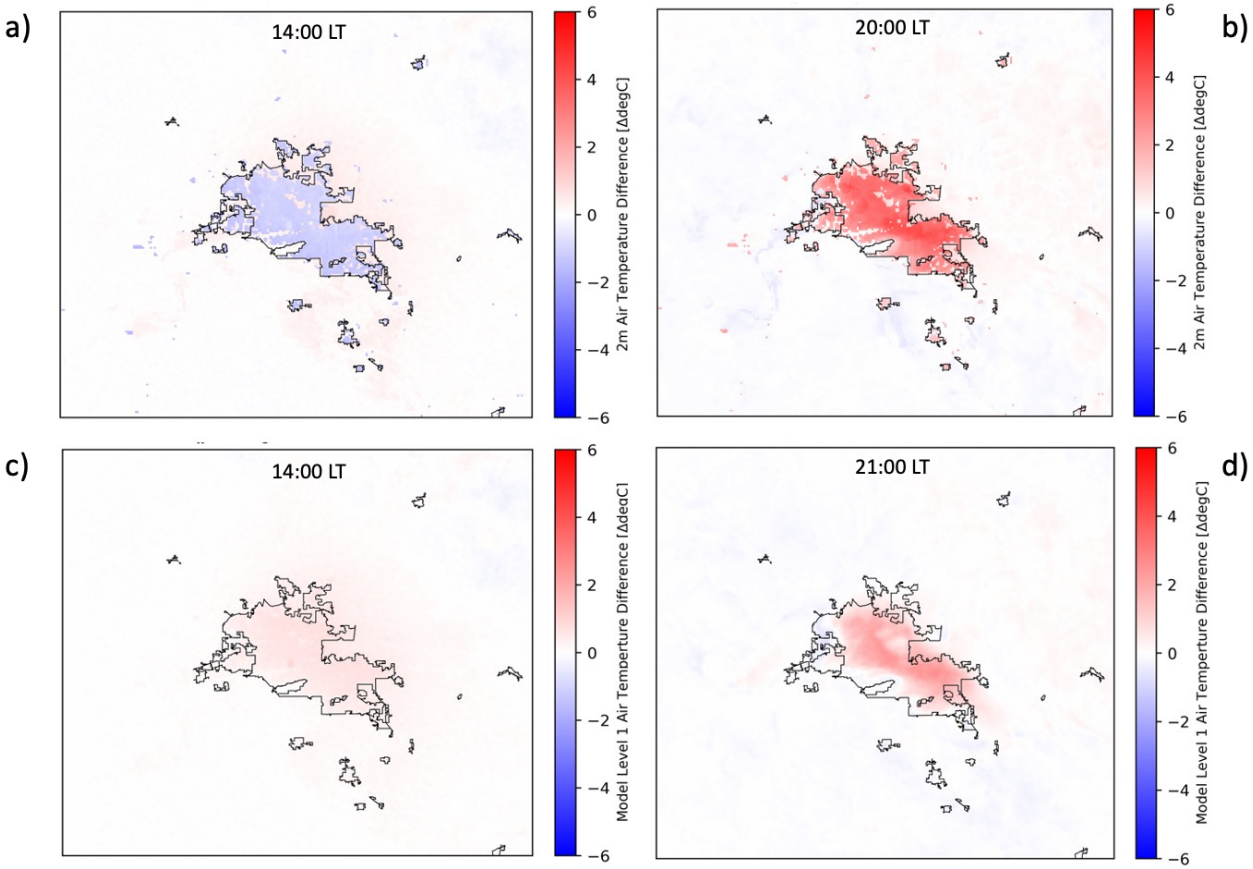

Fig. 9 JJA averaged differences between the *Control* and the *Pre-Settlement* scenarios of 2m air temperature at **a)** 2:00 PM LT and **b)** 8:00 PM LT. **c)** and **d)** as **a)** and **b)** but at the mass center of the first model level (i.e., 25 m AGL).

Due to its weakness, this UBLHI is not able to induce a characteristic circulation. However, it interacts with the background flow, modulating wind speed up and downwind of the metropolitan area. During daytime, especially during the late morning hours (10:00 to 11:00 AM LT) wind flow remains mostly undisturbed within the city along an approximate NW-SE oriented axis. Simultaneously, as the UBLHI forcing coincides with or opposes the southwesterly up-valley flow, areas of approximately 1 m/s wind speed increase and decrease emerge at the southwest and northeast edges of the metropolitan area, respectively (Fig. 6b and Fig. 8d). During the afternoon the drag effect over the urban area creates areas of wind speed increase at the NW and SSW sides of the urban area and a wide area of downwind speed decrease to the northeast (Fig. 6c).

513 At nighttime the interplay becomes somewhat more complicated. While most of the urban
514 environment, especially across its southeastern half, obstructs the southeasterly katabatic flow, a
515 patch of increased wind speed first appears as a reinforcement of the local down-slope flow
516 along the northeast facing flank of the mountain ranges to the southwest of the metro area at
517 around 1:00 AM LT (not shown). As the down-slope drainage loses intensity, at 3:00 AM the
518 UBLHI promotes wind speed increase along a narrow strip on the west part of Metro Phoenix
519 (gold area in Fig. 10a). This induced acceleration extends and intensifies in the air aloft upwards
520 to ~ 500 m AGL, slightly reinforcing the katabatic flows coming from both the east and the west
521 (Fig. 10b).
522 The nighttime UHI of the PMA, by increasing the weak local westerly downslope flow,
523 opposes the main easterly katabatic winds and shifts the point of mass convergence eastward by
524 a few tens of kilometers compared to the *Pre-Settlement* scenario (Fig. 10b, c). This impact
525 reaches its peak intensity at 3:00 AM LT and decreases in magnitude afterwards. As the
526 katabatic wind regime strengthens, cooler air drains into the urban environment, decreasing the
527 UHI intensity and eventually takes over the entire valley near sunrise (i.e., 6:00 AM LT; Fig.
528 5d). The process just described fully unfolds only along a rather narrow stretch of the PMA,
529 roughly ranging between latitudes 33.40^{o}N and 33.50^{o}N where the extent and degree of
530 urbanization is greatest (featuring the only few high-rise districts of the PMA, as well as the Sky
531 Harbor International Airport) and no topographic obstruction to wind flow to the west is present.
532 To the north and south of this narrow band, a combination of reduced urban extent and a more
533 complex terrain prevents the formation and growth of any significant local circulation.
534

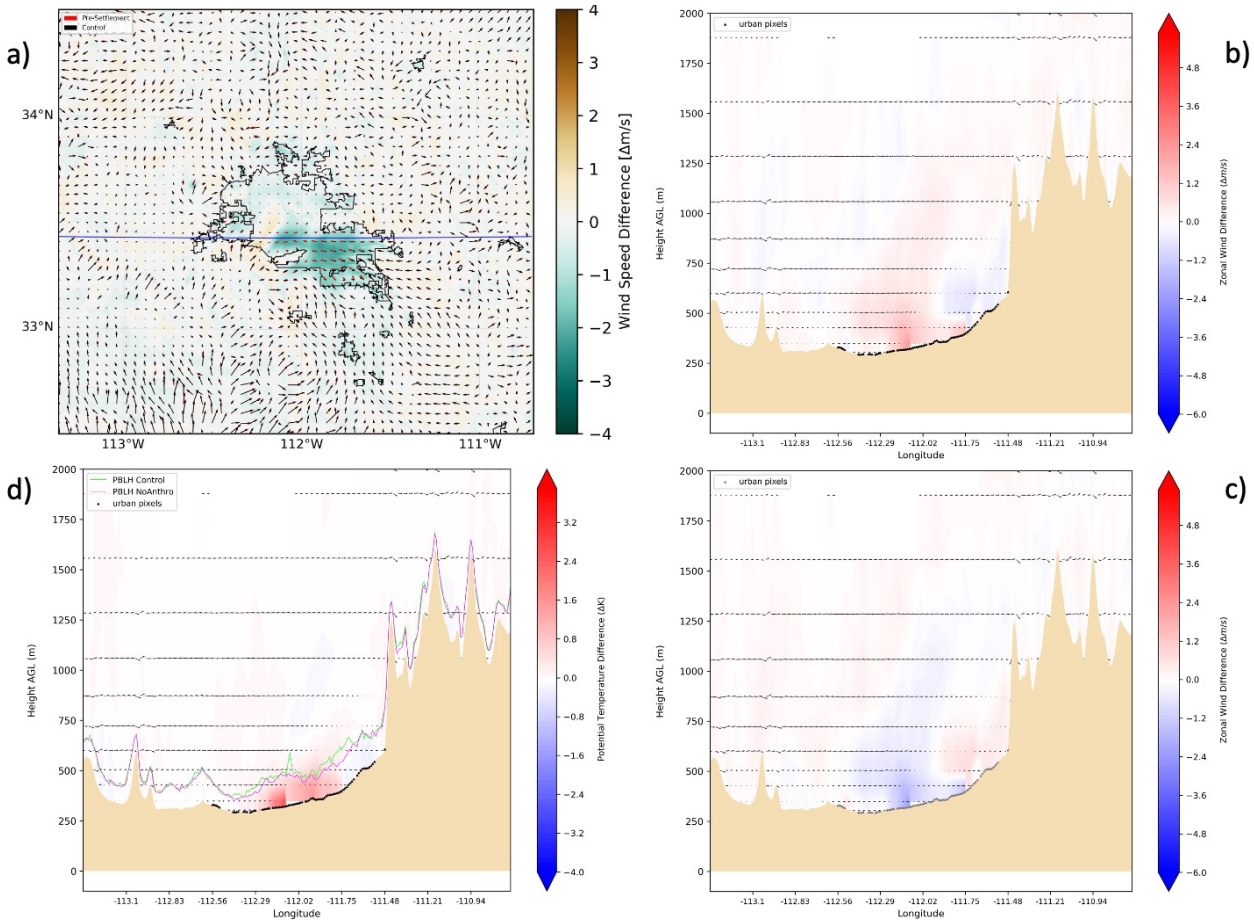

Fig. 10 Wind speed and potential temperature average differences at the time (3:00 AM LT) of maximum intensity of the UBLHI induced circulation. **a)** JJA average of wind vectors at the first model level (25 m AGL) from the *Control* (black arrows) and *Pre-Settlement* (red arrows) scenarios. Color shading represents the JJA average wind speed difference between *Control – Pre-settlement* scenarios. Blue line represents the 33.43°N latitude transect. **b)** Cross section of JJA averaged zonal (U) and vertical (W) wind components from the *Control* scenario. Color shading represents the JJA averaged U component difference between *Control – Pre-settlement* scenarios. **c)** Cross section of JJA averaged zonal (U) and vertical (W) wind components from the *Pre-settlement* scenario. Color shading represents the JJA averaged U component difference between *Pre-settlement – Control* scenarios. **d)** Cross section of JJA averaged zonal (U) and vertical (W) wind components from the *Control* scenario. Color shading represents the JJA averaged potential temperature difference between *Control – Pre-settlement* scenarios. Green line represents JJA averaged PBL top from the *Control* scenario. Purple line represents JJA averaged PBL top from the *Pre-settlement* scenario. **b)**, **c)**, **d)**: the vertical wind (W) component is multiplied by 10 to enhance its magnitude. Black triangles represent the urban pixels along the transect.

552 *3.5 Sensitivity to meteorological conditions*

553

554 Finally, we examine how meteorological conditions modulate the interplay between the PMA
555 UBL and the thermo-topographical circulation of the local complex terrain. Drawing on the
556 results of our model evaluation (Fig. 4), we select four different case study periods representing a
557 variety of meteorological conditions (namely: the warmest, coolest, windiest and calmest
558 summer day) at times when comparison between model results and observations shows the best
559 agreement. We then recalculate and average wind speed differences between the Control and
560 Pre-Settlement scenario across 48-hour time slots centered on each selected day.

561 On June 7th, the coolest day of the summer of 2020 with an average 2 m air temperature of
562 27^{o}C (Fig. 4a), the overall impact of the nighttime UHI is smaller than average, likely as a
563 consequence of reduced heat storage and air conditioning usage. Westerly winds along the
564 33.43^{o}N transect are weak while the easterly katabatic flow is stronger and the center of mass
565 convergence is hard to identify due to flow stagnation (Fig. 11a). The opposite happens on
566 August 14th, the hottest day with an average 2 m air temperature of 38^{o}C (Fig. 4a). On this day,
567 at 3:00 AM and along 33.43^{o}N latitude the westerly flow is considerably strengthened by the
568 nighttime UHI and opposes a weaker easterly katabatic flow, thus resulting in a further eastward
569 shift of the center of mass convergence compared to the JJA average (Fig. 11b). June 30th, our
570 calmest case study day with surface level wind speed ranging between 2.5 and 3.5 m/s (Fig. 4b),
571 features the strongest easterly katabatic flow. Westerly flow along the 33.43^{o}N transect below
572 350 m AGL is virtually non-existent, thus relocating mass convergence towards the western
573 fringes of the PMA (Fig. 10d). Finally, we examine the wind field during the 48-hour period
574 centered on June 8th (windiest day). Near surface wind speed peaks at 8 m/s (Fig. 4b) and the
575 situation is rather similar to the coolest case study day with slightly weaker westerly flow and a
576 slightly stronger easterly katabatic flow (Fig. 11c). This similarity is likely a consequence of the
577 overlapping period of time between this case study period and the coolest day case study, as the
578 cooler temperature period extends until June 11th (Fig. 4a).

579

580

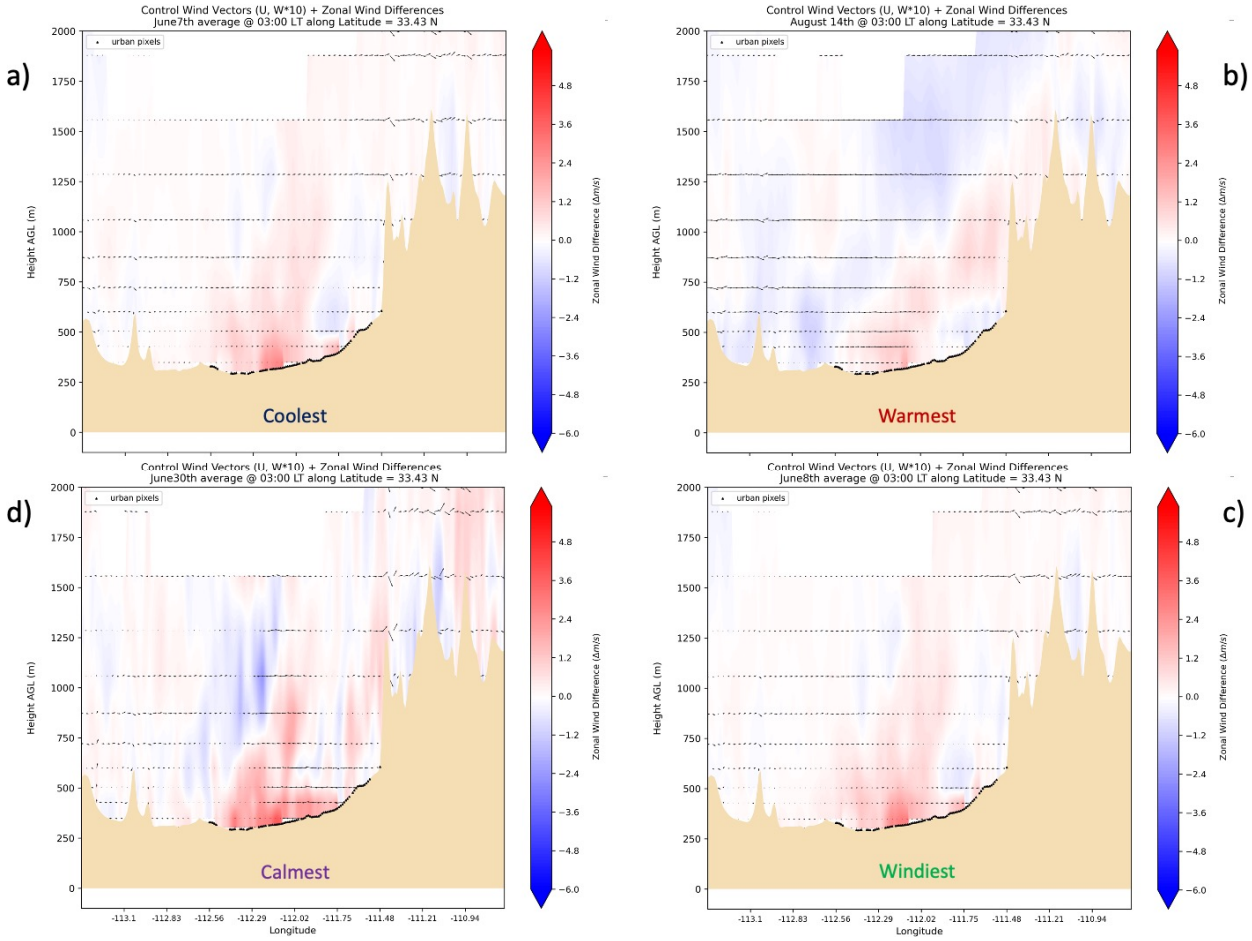

Fig. 11 Wind speed average differences at the time (3:00 AM LT) of maximum intensity of the UBLHI induced circulation along the 33.43°N latitude transect for the four case-study limit meteorological conditions. **a)** Cross section of JJA averaged zonal (U) and vertical (W) wind components (black arrows) from the *Control* scenario and the JJA averaged U component difference between *Control – Pre-settlement* (Color shading) scenarios during the coolest day of summer 2020 (June 7th). **b)** Cross section of JJA averaged zonal (U) and vertical (W) wind components (black arrows) from the *Control* scenario and the JJA averaged U component difference between *Control – Pre-settlement* (Color shading) scenarios during the warmest day of summer 2020 (August 14th). **c)** Cross section of JJA averaged zonal (U) and vertical (W) wind components (black arrows) from the *Control* scenario and the JJA averaged U component difference between *Control – Pre-settlement* (Color shading) scenarios during the windiest day of summer 2020 (June 8th). **d)** Cross section of JJA averaged zonal (U) and vertical (W) wind components (black arrows) from the *Control* scenario and the JJA averaged U component difference between *Control – Pre-settlement* (Color shading) scenarios during the calmest day of summer 2020 (June 30th).

4. Conclusions and Discussion

In this study we used a set of WRF model 1 km grid spacing simulations to investigate the interaction between the UBL of the PMA (Arizona, U.S.) and the thermal circulation of the complex terrain it resides within using identical summer of 2020 meteorological forcing. To achieve this goal, we use a set of paired simulations representing two different landscape scenarios: the *Control* simulation realistically reproduces the current extent and characteristics of the PMA, while the *Pre-Settlement* simulation represents a scenario where all anthropogenic landscape modifications (urban and agricultural) have been replaced with the dominant natural land cover of the arid terrain. Our *Control* simulation results are in good agreement with ground and satellite observations of air and land surface temperature, as well as wind speed and direction, confirming the WRF model's ability to appropriately represent the atmospheric dynamics of urban environments in complex terrain. We then compared simulation results from both scenarios to assess the urban impact on the local wind flow, quantifying differences in the diurnal cycle of wind speed and direction, sensible heat fluxes and TKE.

Our analysis shows that the thermo-topographical circulation characterized by the alternation of anabatic and katabatic wind flow regimes typical of complex terrain dominates in both scenarios. The anabatic regime reaches its maximum intensity at 11:00 AM LT and approaches flow reversal at 7:00 PM LT. Katabatic flows first appear along the steep slopes of the Mogollon Rim at 9:00 PM LT and increase in intensity throughout the night, reaching peak intensity at 6:00 AM LT when all drainage flows merge in the central part of the valley. The morning and evening transitions between the two regimes occur at 8:00 AM and 7:00 PM LTs, respectively, and are characterized by slow winds and a lack of consistent wind directions.

In this context, the PMA behaves as a physical barrier obstructing wind flow in the ISL during most of the day. Its impact on flow affects mostly wind speed with no relevant modification to wind direction. Wind speed reduction ranges between -1.5% (-0.1 m/s) of the background wind speed at 12:00 PM LT and -46% (-1 m/s) at 6 AM LT, and is modulated by the diurnal evolution of urban sensible heat flux excess. During the late morning and early afternoon, a surplus of sensible heat flux promotes deep UBLs and strong vertical mixing that dilutes the aerodynamic resistance associated with the greater urban surface roughness. As urban sensible heat flux decreases in the late afternoon and early evening, wind speed deceleration increases to -30% (-

1.5 m/s) and continues increasing throughout the night as wind speed decreases and opposing katabatic flows collide over the urban area.

We find no evidence of an urban wind island effect over the PMA, as observed in other cities (Droste et al., 2018). The shallow urban canopy layer of the PMA produces a weak (+0.5 K ca.) UHI effect in the ISL throughout the diurnal cycle. Our simulation results indicate that a well-defined UHIC extending into the mixed layer does not develop at any point through the diurnal cycle. However, differential heating between the urban and rural ISL reinforces and opposes wind flow upwind and downwind of the city, both during daytime and nighttime. During the daytime, when the background flow is consistently southwesterly across the entire region, this differential interaction results in both wind speed increase and decrease of up to 50% (~1 m/s) of the background flow upwind and downwind of the metropolitan area, respectively. During nighttime, the UBLHI effect is not able to substantially alter wind flow over the urban area, but at 3-4:00 AM LT, by lightly strengthening inflow from surrounding areas, it appears to shift the center of mass convergence between the strong easterly katabatic flow and the residual weak westerly flow further eastward compared to the *Pre-Settlement* scenario.

To further investigate the role of background meteorology in this interaction, we examined the nighttime UBLHI impact on wind circulation on four different case study days. Within the study period, we chose 4 days each representing one of the following conditions: highest 2 m air temperature, lowest 2 m air temperature, greatest wind speed and lowest wind speed. Background thermal conditions appear to play a greater role than background wind speed in modulating the interaction between local circulations. Lower background temperatures further reduce the impact of the UBLHI on opposing wind flows and mass convergence shift, while higher 2 m air temperature increases it.

As a final consideration, we acknowledge that our conclusions are limited by two key factors. First, the systematic nighttime cold bias emerging from the model evaluation may have resulted in an underestimation of the nighttime UBLHI and associated circulation (i.e., the vertical extent of the UHIC may be somewhat greater than simulated here). We partly addressed this concern in the calibration phase of the model configuration through modification of relevant biophysical properties (e.g., increasing the thermal capacity and lowering the emissivity of urban surfaces using commonly accepted values drawn from the material engineering literature). However, the impact of these modifications, although effective, proved to be insufficient. A second limiting

660 factor could be the lack of an irrigation scheme implementation of green spaces and croplands.
661 Added moisture in the urban environment is likely to lead to increased nighttime temperatures,
662 resulting from enhanced downward longwave radiation, further decreasing the nighttime
663 systematic bias noted here. However, in our model configuration, the increased soil moisture of
664 irrigated croplands is partially accounted for by a lower albedo, and the difference in LULC
665 between scenarios is considered to be a meaningful representation of relevant biophysical
666 characteristics.

667 With this study we fill a gap in the current existing literature, as the majority of wind studies
668 in urban environments focus on flow/building interactions within the urban canopy layer at the
669 building or neighborhood scale using computational fluid dynamics models or observations.
670 Here, we focused on the impact of a fast-growing metropolitan area on wind flow in the UBL, to
671 improve the understanding of land-atmosphere interactions in urban environments from a
672 regional climate perspective. Such understanding can be societally beneficial, for example, by
673 improving aviation operation and by helping to inform planning and policy decisions to address
674 concerns related with pollutant transport and dispersion. Such concerns are especially important
675 in a semi-desert environment like southern Arizona where dust and ozone pollution are important
676 societal pressures, but may be similarly important across other urban environments situated
677 within or surrounded by complex terrain (e.g., Salt Lake City, UT; Las Vegas, NV; Tehran,
678 Iran). Extending our analysis to cities with different morphologies and different geographical
679 settings will help situate our results in a broader framework.

Acknowledgements

The data produced for this study are available at the ASU Library Research Data Repository https://dataverse.asu.edu/

The authors acknowledge the large-scale, high-performance and high-throughput computing support from Research Computing at Arizona State University. https://asurc.atlassian.net/wiki/spaces/RC/overview

The authors have no conflict of interest to disclose.

References

Balling Jr, R. C., & Cerveny, R. S. (1987). Long-term associations between wind speeds and the urban heat island of Phoenix, Arizona. *Journal of Applied Meteorology and Climatology*, *26*(6), 712-716.

Balling, R., & Brazel, S. W. (1988). High-resolution surface temperature patterns in a complex urban terrain. *Photogrammetric engineering and remote sensing*, *54*(9), 1289-1293.

Blumen, W. (Ed.). (2016). *Atmospheric processes over complex terrain* (Vol. 23). Springer.

Bornstein, R. D., & Johnson, D. S. (1977). Urban-rural wind velocity differences. *Atmospheric Environment (1967)*, *11*(7), 597-604.

Brazel, A. J., Fernando, H. J. S., Hunt, J. C. R., Selover, N., Hedquist, B. C., & Pardyjak, E. (2005). Evening transition observations in Phoenix, Arizona. *Journal of Applied Meteorology and Climatology*, *44*(1), 99-112.

Brown, P. and Russell, B. (1987-1995). Weather Data and On-Line Documentation. *The Arizona Meteorological Network (AZMET) Computer Bulletin Board. The University of Arizona Cooperative Extension Service, Tucson, AZ.*

Bureau, U. C. (2019). City and town population totals: 2010-2019. *The United States Census Bureau*.

Burian, S. J., Velugubantla, S. P., & Brown, M. J. (2002). Morphological analyses using 3D building databases: Phoenix, Arizona. *Los Alamos National Laboratory*.

Cenedese, A., & Monti, P. (2003). Interaction between an inland urban heat island and a sea-breeze flow: A laboratory study. *Journal of Applied Meteorology and Climatology*, *42*(11), 1569-1583.

Chandler, T. J. (1960). Wind as A Factor of Urban Temperatures—A Survey in North-East London. *Weather*, *15*(6), 204-213.

Chen, F., & Dudhia, J. (2001). Coupling an advanced land surface–hydrology model with the Penn State–NCAR MM5 modeling system. Part I: Model implementation and sensitivity. *Monthly weather review*, *129*(4), 569-585.

Chen, X., Jeong, S., Park, H., Kim, J., & Park, C. R. (2020). Urbanization has stronger impacts than regional climate change on wind stilling: a lesson from South Korea. *Environmental Research Letters*, *15*(5), 054016.

Chow, W. T., Brennan, D., & Brazel, A. J. (2012). Urban heat island research in Phoenix, Arizona: Theoretical contributions and policy applications. *Bulletin of the American Meteorological Society*, *93*(4), 517-530.

Droste, A. M., Steeneveld, G. J., & Holtslag, A. A. (2018). Introducing the urban wind island effect. *Environmental Research Letters*, *13*(9), 094007.

Esri, R. (2011). ArcGIS desktop: release 10. *Environmental Systems Research Institute, CA*.

Fernando, H. J. S., Lee, S. M., Anderson, J., Princevac, M., Pardyjak, E., & Grossman-Clarke, S. (2001). Urban fluid mechanics: air circulation and contaminant dispersion in cities. *Environmental Fluid Mechanics*, *1*(1), 107-164.

Fernando, H. J. S. (2010). Fluid dynamics of urban atmospheres in complex terrain. *Annual review of fluid mechanics*, *42*, 365-389.

Fernando, H. J., Verhoef, B., Di Sabatino, S., Leo, L. S., & Park, S. (2013). The Phoenix evening transition flow experiment (TRANSFLEX). *Boundary-layer meteorology*, *147*(3), 443-468.

Findlay, B. F., & Hirt, M. S. (1969). An urban-induced meso-circulation. *Atmospheric Environment (1967)*, *3*(5), 537-542.

Foroutan, H., & Pleim, J. E. (2017). Improving the simulation of convective dust storms in regional-to-global models. *Journal of advances in modeling earth systems*, *9*(5), 2046-2060.

Ganbat, G., Baik, J. J., & Ryu, Y. H. (2015). A numerical study of the interactions of urban breeze circulation with mountain slope winds. *Theoretical and Applied Climatology*, *120*, 123-135.

Georgescu, M., Miguez-Macho, G., Steyaert, L. T., & Weaver, C. P. (2008). Sensitivity of summer climate to anthropogenic land-cover change over the Greater Phoenix, AZ, region. *Journal of arid environments*, *72*(7), 1358-1373.

Georgescu, M., Miguez-Macho, G., Steyaert, L. T., & Weaver, C. P. (2009a). Climatic effects of 30 years of landscape change over the Greater Phoenix, Arizona, region: 1. Surface energy budget changes. *Journal of Geophysical Research: Atmospheres*, *114*(D5).

Georgescu, M., Miguez-Macho, G., Steyaert, L. T., & Weaver, C. P. (2009b). Climatic effects of 30 years of landscape change over the Greater Phoenix, Arizona, region: 2. Dynamical and thermodynamical response. *Journal of Geophysical Research: Atmospheres*, *114*(D5).

Georgescu, M., Moustaoui, M., Mahalov, A., & Dudhia, J. (2011). An alternative explanation of the semiarid urban area "oasis effect". *Journal of Geophysical Research: Atmospheres*, *116*(D24).

Giovannini, L., Zardi, D., de Franceschi, M., & Chen, F. (2014). Numerical simulations of boundary-layer processes and urban-induced alterations in an Alpine valley. *International Journal of Climatology*, *34*(4), 1111-1131.

Gorelick, N., Hancher, M., Dixon, M., Ilyushchenko, S., Thau, D., & Moore, R. (2017). Google Earth Engine: Planetary-scale geospatial analysis for everyone. *Remote sensing of Environment*, *202*, 18-27.

Grawe, D., Thompson, H. L., Salmond, J. A., Cai, X. M., & Schlünzen, K. H. (2013). Modelling the impact of urbanisation on regional climate in the Greater London Area. *International Journal of Climatology*, *33*(10), 2388-2401.

Haeger-Eugensson, M., & Holmer, B. (1999). Advection caused by the urban heat island circulation as a regulating factor on the nocturnal urban heat island. *International Journal of Climatology: A Journal of the Royal Meteorological Society*, *19*(9), 975-988.

Hou, A., Ni, G., Yang, H., & Lei, Z. (2013). Numerical analysis on the contribution of urbanization to wind stilling: an example over the greater Beijing metropolitan area. *Journal of applied meteorology and climatology*, *52*(5), 1105-1115.

Janić, Z. I. (2001). Nonsingular implementation of the Mellor-Yamada level 2.5 scheme in the NCEP Meso model.

Jin, S., Dewitz, J., Danielson, P., Granneman, B., Costello, C., Zhu, Z., & Smith, K. (2021, December). National Land Cover Database 2019: A new strategy for creating clean Landsat composite images. In *AGU Fall Meeting Abstracts* (Vol. 2021, pp. B35D-1467).

Kratzer, A. (1956). *The Climate of Cities:(Das Stadtklima)*. US Department of Commerce Clearinghouse.

Laloui, L., & Loria, A. R. (2019). *Analysis and design of energy geostructures: theoretical essentials and practical application*. Academic Press.

Li, J., Georgescu, M., Hyde, P., Mahalov, A., & Moustaoui, M. (2015). Regional-scale transport of air pollutants: impacts of Southern California emissions on Phoenix ground-level ozone concentrations. *Atmospheric Chemistry and Physics*, *15*(16), 9345-9360.

Li, Z., Yu, X., Liang, Y., & Wu, S. (2021). Carbon nanomaterials for enhancing the thermal, physical and rheological properties of asphalt binders. *Materials*, *14*(10), 2585.

Martilli, A., Clappier, A., & Rotach, M. W. (2002). An urban surface exchange parameterisation for mesoscale models. *Boundary-layer meteorology*, *104*, 261-304.

McVicar, T. R., Roderick, M. L., Donohue, R. J., Li, L. T., Van Niel, T. G., Thomas, A., ... & Dinpashoh, Y. (2012). Global review and synthesis of trends in observed terrestrial near-surface wind speeds: Implications for evaporation. *Journal of Hydrology*, *416*, 182-205.

Mellor, G. L., & Yamada, T. (1982). Development of a turbulence closure model for geophysical fluid problems. *Reviews of Geophysics*, *20*(4), 851-875.

Mesinger, F., DiMego, G., Kalnay, E., Mitchell, K., Shafran, P. C., Ebisuzaki, W., ... & Shi, W. (2006). North American regional reanalysis. *Bulletin of the American Meteorological Society*, *87*(3), 343-360.

Monti, P., Fernando, H. J. S., Princevac, M., Chan, W. C., Kowalewski, T. A., & Pardyjak, E. R. (2002). Observations of flow and turbulence in the nocturnal boundary layer over a slope. *Journal of the Atmospheric Sciences*, *59*(17), 2513-2534.

Nadolski, V. L. (1998). Automated surface observing system (ASOS) user's guide. *National Oceanic and Atmospheric Administration, Department of Defense, Federal Aviation Administration, United States Navy*, *20*.

Niu, G. Y., Yang, Z. L., Mitchell, K. E., Chen, F., Ek, M. B., Barlage, M., ... & Xia, Y. (2011). The community Noah land surface model with multiparameterization options (Noah-MP): 1. Model description and evaluation with local-scale measurements. *Journal of Geophysical Research: Atmospheres*, *116*(D12).

NOAA National Centers for Environmental information, Climate at a Glance: City Time Series, published February 2023, retrieved on February 14, 2023 from https://www.ncei.noaa.gov/access/monitoring/climate-at-a-glance/city/time-series

Ohashi, Y., & Kida, H. (2002). Effects of mountains and urban areas on daytime local-circulations in the Osaka and Kyoto regions. *Journal of the Meteorological Society of Japan. Ser. II*, *80*(4), 539-560.

Oke TR (1982) The energetic basis of the urban heat island. Q J R Meteorol Soc 108(455):1–24

Papanastasiou, D. K., Melas, D., & Lissaridis, I. (2010). Study of wind field under sea breeze conditions; an application of WRF model. *Atmospheric Research*, *98*(1), 102-117.

Peng, L., Liu, J. P., Wang, Y., Chan, P. W., Lee, T. C., Peng, F., ... & Li, Y. (2018). Wind weakening in a dense high-rise city due to over nearly five decades of urbanization. *Building and Environment*, *138*, 207-220.

Pielke, R. A., Cotton, W. R., Walko, R. E. A., Tremback, C. J., Lyons, W. A., Grasso, L. D., ... & Copeland, J. H. (1992). A comprehensive meteorological modeling system—RAMS. *Meteorology and atmospheric Physics*, *49*(1), 69-91.

Puliafito, S. E., Allende, D. G., Mulena, C. G., Cremades, P., & Lakkis, S. G. (2015). Evaluation of the WRF model configuration for Zonda wind events in a complex terrain. *Atmospheric Research*, *166*, 24-32.

Rafailidis, S. (1997). Influence of building areal density and roof shape on the wind characteristics above a town. *Boundary-layer meteorology*, *85*, 255-271.

Ryu, Y. H., & Baik, J. J. (2013). Daytime local circulations and their interactions in the Seoul metropolitan area. *Journal of Applied Meteorology and Climatology*, *52*(4), 784-801.

Salamanca, F., Krpo, A., Martilli, A., & Clappier, A. (2010). A new building energy model coupled with an urban canopy parameterization for urban climate simulations—part I. formulation, verification, and sensitivity analysis of the model. *Theoretical and applied climatology*, *99*, 331-344.

Salamanca, F., Zhang, Y., Barlage, M., Chen, F., Mahalov, A., & Miao, S. (2018). Evaluation of the WRF-urban modeling system coupled to Noah and Noah-MP land surface models over a semiarid urban environment. *Journal of Geophysical Research: Atmospheres*, *123*(5), 2387-2408.

Savijärvi, H., & Liya, J. (2001). Local winds in a valley city. *Boundary-layer meteorology*, *100*, 301-319.

Sharma, A., Wuebbles, D. J., & Kotamarthi, R. (2021). The need for urban-resolving climate modeling across scales. *AGU Advances*, *2*(1), e2020AV000271.

Shreffler, J. H. (1979). Heat island convergence in St. Louis during calm periods. *Journal of Applied Meteorology and Climatology*, *18*(12), 1512-1520.

Skamarock, W. C., Klemp, J. B., Dudhia, J., Gill, D. O., Liu, Z., Berner, J., ... & Huang, X. Y. (2019). A description of the advanced research WRF model version 4. *National Center for Atmospheric Research: Boulder, CO, USA*, *145*(145), 550Toro, R., Kvakić, M., Klaić, Z. B., & Koračin, D. (2019). Exploring atmospheric stagnation during a severe particulate matter air pollution episode over complex terrain in Santiago, Chile. *Environmental pollution*, *244*, 705-714.

Toro, R., Kvakić, M., Klaić, Z. B., & Koračin, D. (2019). Exploring atmospheric stagnation during a severe particulate matter air pollution episode over complex terrain in Santiago, Chile. *Environmental pollution*, *244*, 705-714.

Vera, C., Higgins, W., Amador, J., Ambrizzi, T., Garreaud, R., Gochis, D., ... & Zhang, C. (2006). Toward a unified view of the American monsoon systems. *Journal of climate*, *19*(20), 4977-5000.

Wan, Z., Hook, S., Hulley, G. (2021). *MODIS/Terra Land Surface Temperature/Emissivity Daily L3 Global 1km SIN Grid V061* [Data set]. NASA EOSDIS Land Processes DAAC. Accessed 2023-02-24 from https://doi.org/10.5067/MODIS/MOD11A1.061

Wang, J., Feng, J., Yan, Z., & Zha, J. (2020). Urbanization impact on regional wind stilling: A modeling study in the Beijing-Tianjin-Hebei region of China. *Journal of Geophysical Research: Atmospheres*, *125*(20), e2020JD033132.

Wu, S., Wang, Y., Chen, C., Cao, Z., Cao, J., Yu, Z., & Song, H. (2021). Valley city ventilation under the calm and stable weather conditions: A review. *Building and Environment*, *194*, 107668.